TOC

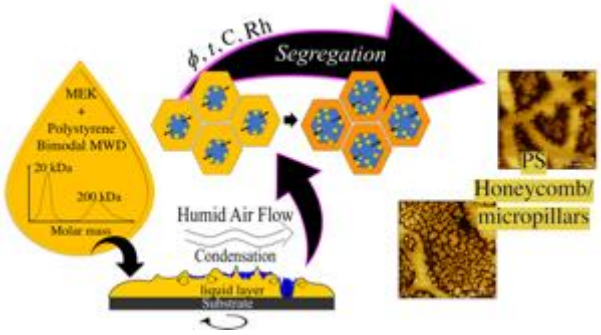

The interplay between bi-modal molecular weight distribution in polystyrene and humidity induces self-assembly of biomimetic micropillars/honeycomb morphology in the thin polymer film

Authors: Maciej Łojkowski[1,*], Adrian Chlanda[1,2], Emilia Choińska[1], Wojciech Swieszkowski[1*].

Affiliation:

1. Faculty of Material Sciences and Engineering, Warsaw University of Technology, Wołoska 141, 02-507 Warsaw, Poland
2. Department of Chemical Synthesis and Flake Graphene, Łukasiewicz Research Network - Institute of Microelectronics and Photonics, Aleja Lotników 32/46, 02-668 Warsaw, Poland.

Abstract

Segregation of polymer chains of different molecular weights is a well-known process. A traditional experimental approach of studying phase segregation in thin films composed of polymer blends with identical chemical compositions but different molecular weights was focused on functionalisation of chemical group or modification of end-group. In this study, however, a different approach was proposed. Polystyrene with bimodal molecular weight distribution, but no additional chemical modification was used. The films were prepared by

spin-coating and the segregation between polystyrene phases was investigated by force spectroscopy. The solubility of bimodal polystyrene was explored. At the right molecular weight distribution and soluted in Methyl Ethyl Ketone, the phase segregation occurred. Introduction of moist airflow induced the separation of the lower molecular weight into micropillars and the heavier fraction self-organized into a honeycomb. As a result, an easy, fast, and effective method of obtaining micropillar/honeycomb morphologies was demonstrated. The mechanism of formation of such structures was explained.

Keywords

self-assembly; polymer thin films; bimodal molecular weight distribution; polystyrene; spin-coating; micro-pillars; honeycomb; breath-figures; liquid-liquid phase separation;

Introduction

Biomimetic complex morphologies compromising micropillars have gained attention due to their wide range of possible applications, for example, their special wetting properties (1,2), application in studying biofilm formation (3), or controlling stem cells differentiation (4). Two widespread methods which allow the creation of a broad range of structures of polymer thin films (PTFs) are spin-coating (5) and breath figures (6). These methods were applied for manufacturing organic ferroelectric switches (7), light-emitting devices (8), sensors (9,10), drug delivery systems (11,12), biologically active surfaces (13,14), functional nanostructured surfaces (15,16), and membranes (17). Both these processes rely heavily on the interaction dynamics between the solvent, the polymer, and the vapours in the vicinity of the surface. During spin-coating, a droplet of a mixture of a solvent and one or two polymers is dropped onto the substrate. Subsequently, the substrate is rotated very quickly to cover it uniformly with the solution's liquid film. As a result, the solvent evaporates. Thus, solvent and temperature

quench occurs. The change of the solvent volume and temperature often leads to unintentional or intentional liquid-liquid phase separation. (18) It has been argued that such phase separation often starts in the early stages of spinning. (18,19) The further spinning of the solution leads to gel formation, which eventually slows down the diffusion inside the film. As a result, the occurring morphology becomes frozen in time before reaching an equilibrium. The time necessary for the morphology to stop evolving depended on such factors as the solvent evaporation rate, solution viscosity, or spinning rate. (20,21) In the second technique mentioned above, the breath figures appear on the liquid film's surface when the humid airflow accelerates the evaporation rate. Successively, the temperature decreases, which results in nucleation and growth of water droplets. These droplets create the regular honeycomb array of cavities in the film. After most of the solvent had evaporated, the temperature increases to that of the surroundings, the droplets evaporate, leaving a porous surface. The start of these droplets' nucleation is governed by the onset time related to the solvent evaporation rate, solution concentration, and airflow.(22)

The factors which regulate the final morphology, like the solvent type (23), concentration(24), the spinning rate (21), and blend composition (25,26), were already intensively studied. However, the effect of molecular weight distribution (MWD) is still not well understood. Regarding the subject of the PTFs, scientific literature focuses mostly on polymers with narrow MWD. Conversely, Wu et al. have studied the effect of MWD on the self-assembly of end-functionalised polystyrenes. They proposed a new way of controlling the morphology of PTF obtained via breath figures by changing the MWD width. As a result, the porous membrane with higher robustness was obtained.(27)

Therefore, it should be highlighted that the location and the width of the MWD can affect polymer solution properties and, as a result, solid thin polymeric film formation. The width of the MWD can be tailored either within the polymerisation process (28,29) or by mixing two

polymer species with very narrow MWD (30). By tailoring the concentration and location of the two nodes of the distribution of a bimodal polymer, it is possible to achieve unique properties.(31) For example, Heitmiller et al. have reported that the heterogeneous melt of polyethylene had a higher flow index than the homogeneous one.(32) The investigation performed by Koningsveld et al. has shown that the bimodal MWD has got a significant effect on the liquid-liquid binodal curve of polymers in solution. (33) Phase regions characterise such solution, and liquid-liquid phase separation between polymer- and solvent-rich fractions can occur. Zeman et al. have demonstrated that the critical concentration enabling phase separation in a solution of two polymer species decreases with an increase in the molecular weight M_w.(34) Moreover, even when the polymer-polymer interactions are athermal, i.e. Flory-Huggins interaction parameter χ equals zero, the phase separation can occur due to the large difference in entropy between long and short chains, which act as separate entities and influences the viscosity of bimodal solutions.(35) Harris et al. have found that the viscosity of the blend of bimodal polystyrene can be considered as a sum of components.(36) It has been discussed that blending polystyrenes with different molecular weights mixed the entanglement types between polymer chains. Furthermore, it was presented that the polymers' concentration in the solvent changes how the polymer chains interact. It was found that two polymer chains with the same monomer chemical structure would act as two different polymers, provided that the concentration is below the overlap concentration (C*). However, once the overlap concentration occurs, the polymer's cooperative motion starts, and the behaviour of the solution changes. (37,38)

Successive research focused on studying how the polymer chains of varying lengths segregate in PTF. Hariharan et al. investigated the effect of the entropy of spin-coated and annealed bimodal PTF on polymer chain segregation.(39) It was shown that higher entropy of shorter chains led to their segregation on the PTF surface, while the longer chains' lower entropy

promoted their segregation in bulk. Tanaka et al., in turn, studied spin-coated polystyrenes blends with low and high M_w with narrow MWD utilising toluene as a solvent. They reported that the PTFs consisting of polystyrenes with a low molecular weight demonstrated surface segregation after thermal treatment. (30) Several other recent studies have illustrated the segregation of lower molecular mass elements towards the surface during annealing. (40–44) On the other hand, it has been shown that the deuterated polymer's segregation can change the surface roughness after having annealed the coating. (45–48)

Despite the extensive studies performed on bimodal polymer solutions and melts, the segregation during short time scales, such as during spin-coating, when the solid polymer film is established within few seconds, was not observed until now pristine polystyrene. In the present study, the bimodal PS was combined with MEK as a solvent. MEK is considered a marginal solvent for PS, while it is more hygroscopic then typically used solvents for polystyrene. (49,50) The humid conditions can reduce the solubility of hydrophobic polystyrene when moisture is absorbed. The phase segregation of the low and high molecular weight fractions of polystyrene was studied in function of the humidity. During the spin coating process, the humidity level was precisely controlled, and spin-coating at humidity ranging up to 75% was performed. It was shown that a certain set of conditions leads to a combined honeycomb/micropillars morphology.

The mechanism of the formation of the honeycomb/micropillars was explored. It was shown that the longer and shorter PS chains soluted in the MEK phase segregate. Due to water condensation, a new interface occurred between the moistened substrate and the polymeric solution. At this new interface, the lower molecular weight PS fraction was separated. The heavier molecular fraction reinforced the honeycomb. The force spectroscopy was used to discover the different PS phases. The viscosity investigation gave insight into chain-chain

interactions and solubility. The in-situ reflectometry depicted the evaporation rate and particularities of the evaporation process.

Although the spin-coating was chosen for its ease of controlling the evaporation rate, we believe that the proposed method can be extended to other techniques like dip-coating or ink-jet printing.

2. Experimental

2.1 Materials

All polymers and solvents were purchased from Sigma Aldrich (Merck KGaA). One side polished ultra-smooth SiOx wafers were bought from Technolutions Sp. z o. o.

2.2 Preparation of the coatings

Analytic standard grade polystyrenes (PS) as obtained from the supplier with PDI = 1.04 and M_w = 20 kDa, 91 kDa, 150 kDa, or 200 kDa were used.

Two kinds of blends were prepared: the blends of 20 kDa and 200 kDa PS mixed in 75/25, 50/50, 25/75 w/w % proportions; similarly, the blends of 91 kDa and 200 kDa PS were mixed in the same proportions and dissolved in methyl ethyl ketone (analytic grade, MEK), mixed for an hour at 37 ^{O}C. After mixing, the solutions were stored overnight. The list of polystyrene blends used is summarised in Table 1. The concentrations of these solutions ranged from 2.5 mg/ml to 80 mg/ml. DIY Arduino-based spin-coater with a chamber with controlled humidity was used to spin polystyrene films onto the SiOx wafers. The experimental setup is depicted in Supplementary Information (SI) Fig. S1 – S2. A 35 µl of the solution was pipetted on the 1 cm x 1 cm wafer. The spin-coating was performed in a closed chamber with a constant airflow of 10 ml/min to maintain the desired humidity. The rotational speed was 2700 rpm or 3300 rpm.

The spinning time was set to 10 s to allow the solvent to evaporate. Solutions were spin-coated under humidity of Rh 0%, 45%, 55%, 75%.

Table 1. List of polymer blends that were used for spin-coating.

Type of Blend	Sample code	Molecular weight M_w [kDa]		PDI
Uniform	20 kDa	20		1.04
	91 kDa	91		1.04
	150 kDa	150		1.04
	200 kDa	200		1.04
Bimodal	Sample code	Molecular weight		PDI
		[M_w] [kDa] (1	[M_n] [kDa] (2	
91 kDa / 200 kDa	75/25*	137	118	1.16
	50/50*	166	146	1.14
	25/75*	186	173	1.08
20 kDa / 200 kDa	75/25**	158	65	2.43
	50/50**	184	110	1.67
	25/75**	194	155	1.25

(1 Weight average molecular weight $[M_w] = (f_1M_{w1}^2 + f_2M_{w2}^2)/(f_1M_{w1} + f_2M_{w2})$, *(2 Number average molecular weight* $[M_n] = f_1M_{w1} + f_2M_{w2}$, *where f - fraction of one of the polymers in %; PDI states for the Polydispersity index.*

2.3 Gel permeation chromatography (GPC)

The number and weight average molecular weights (M_n and M_w) were determined by a modular system Agilent 1200 series GPC with a refractive index detector (RID) equipped with two PLgel 5 µm MIXED-C columns (300x7.5 mm) in the series, while polydispersity index was calculated as the ratio of M_w/M_n. Calibration was performed using a set of 12 narrow-distributed polystyrene standards with the molecular weight (M_p) in the range of 474 g/mol - 1 800 000 g/mol.

The measurements were performed at 35 °C. The chloroform GPC grade was used as a solvent at the flow rate of 0.7 ml/min. All samples (~2 mg/ml) were filtered through a PTFE 0.2 µm

membrane before the analysis. The data were collected by ChemStation for LC and analysed by ChemStation GPC Data Analysis Software.

2.4 Force Spectroscopy FS and Elastic Modulus

When a Force Spectroscopy experiment is performed, an AFM probe applies strain on the film surface.(51) Force spectroscopy was performed by means of the atomic force microscope (AFM, Asylum Research MFP3D Bio). (52) OMLCT-AC200TS-R3 (Olympus) cantilever was used with the nominal spring constant k = 9 N/m and the tip radius below 10 nm as suggested by the cantilever's producer. AFM was calibrated using the built-in thermal vibrations method. (53) Johnson, Kendall, and Roberts (JKR) model was used to calculate the elastic modulus (E).(54) The indentation depth was ~8 nm (Supplementary Information, *4. Force Spectroscopy*). As we wanted to neglect the possible influence of stiff (silica) substrate on the polystyrene coating's registered mechanical data, we decided to perform an FS experiment using the thickest films (films spun from the solution of a concentration of 80 mg/ml).

Maps of a large area of the coating 80 μm x 80 μm with 40 x 40 points were obtained. These higher resolution maps are supplemented as an attachment (SI). These data were supported by lower resolution maps with a resolution of 15 x 15 points. Each map was used to obtain the mean elastic modulus value. Altogether, at least five maps were made. Ordinary one-way ANOVA followed by multiple comparisons Fisher's test was used to compare different groups' means.

Furthermore, histograms representing each higher resolution map were prepared. The skewness of the elastic modulus distribution was measured. Skewness was divided into two groups: one for the uniform coatings and one for bimodal coatings. The t-test ($p < 0.05$) was used to compare the means of these two groups.

2.5 Evaluation of thickness of spin-coated films by means of atomic force microscopy

The thickness of spin-coated films was assessed based on the intentionally made scratches' topography images (SI Fig. S3). Five randomly selected areas of each sample were tested, and profiles were generated. Each of the profile lines was averaged from three contiguous lines to avoid any unwanted artefacts.

2.6. Imaging of the coatings

The inverted light microscopes (Nikon EPIPHOT 200 and Zeiss Axio Observer) were used for imaging. The atomic force microscope (AFM, Asylum Research MFP3D Bio) working in the tapping mode (AC mode) was used to illustrate the phase composition and topography of the polystyrene films.

2.7 In-situ measurement of evaporation during spin-coating through laser light reflectometry with stroboscopic effect

In-situ stroboscopic laser light reflectometry was developed to investigate the thinning of the solution layer while spinning. The laser light is reflected from the coating during the spin-coating process. The occurring interference pattern can be used to estimate the thinning rate of the solution. (55–57) Simultaneously, the variability of the amplitude of the degree of reflection ϱ can be used to characterise the emergence of the interfacial instabilities in the coating and roughening of the surface when the coating is spun. (58) The experimental setup is described in SI, Fig. S1 – S2.

Depending on the thickness of the layer, constructive or destructive interference can occur. The condition for the constructive interference was calculated from Bragg's law: $2n\Delta h cos\theta = m\lambda$, where n is the refractive index of the layer, Δh is the thickness of the layer, θ – incident angle, m is an integer number, and λ is the light wavelength. For pure MEK Δh = 235 nm (assuming

the refractive index MEK = 1.3788). For the polymer solution, it was assumed that the refractive index was n = 1.5, thus Δh = 217 nm. The laser light wavelength was λ = 650 nm.

2.8 Data analysis and visualisation

For data visualisation and analysis, GraphPad Prism 8 was used. For image analysis procedures implemented in Gwyddion software (ver 2.50) were used.

2.9 Fourier Transform IR

Infrared spectra were collected using a Fourier transform infrared spectrophotometer (Nicolet 8700 FTIR, Thermo Scientific). Measurements were performed using the FTIR ATR over a range of 4000−400 cm−1.

2.10 Contact Angle and Surface Free Energy Measurement

The contact angle (CA) was measured using a Data Physics OCA 20 goniometer. The contact angle was measured with a sessile drop method. For Surface Free Energy measurement (SFE), two kinds of coatings were chosen: 20 kDa and 200 kDa. For each type of coating, three droplets were measured, and three different coatings were used. Two liquid systems were used: deionised water and diiodomethane (Sigma Aldrich, Analytic grade). The groups were compared with the t-test ($p < 0.05$). Owens, Wendt, Rabel, and Kaelble (OWKR) method was used for SFE calculation. (59)

3. Result and discussion

The solutions with bimodal MWD were prepared so that the two nodes in the distribution were clearly separated. The GPC molecular weight distribution of a single node MWD (uniform) is presented in Fig. 1 A, which illustrates the MWD of 91 kDa polystyrene with narrow

distribution (PDI=1.04). In contrast, Fig. 1 B illustrates the MWD with two nodes of a blend of 91 kDa PS with 200 kDa PS, both with narrow distributions (PDI=1.04).

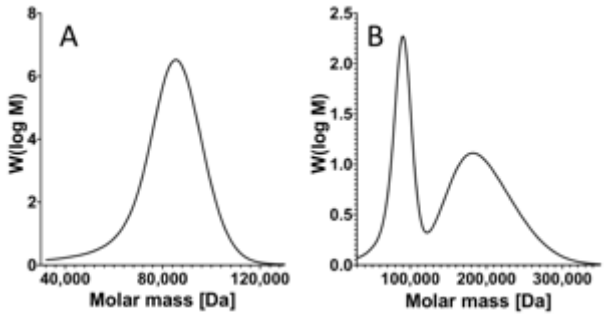

Fig 1. Exemplary GPC experiment results of bimodal and uniform MWD polystyrene; A - narrow uniform MWD, Mw = 91 kDa, PDI 1.04; B – bimodal MWD, blend of Mw = 91 kDa, PDI = 1.04 and Mw = 200 kDa, PDI = 1.04.

The evaporation of the solvent through the spin-coating increased the viscosity of the solution. Successively, the solution concentration fell below the threshold at which the components cannot support coexistence as one phase (Fig 2A and 2B). The arrows mark the paths of the three tested compositions' evaporation: 75/25 w/w%, 50/50, and 25/75, respectively. Due to the dissimilarity of the molecular weight of lighter and heavier elements, the phase diagram is not symmetrical but is shifted towards the heavier element's lower miscibility.(60)

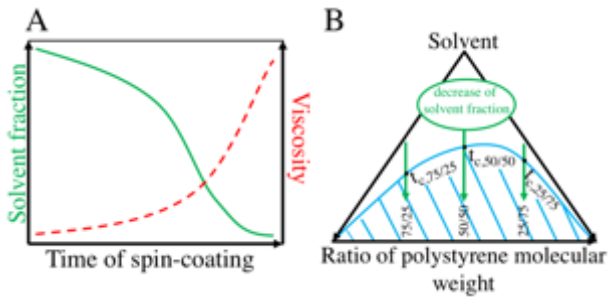

Fig. 2 A – Schematic illustration of the change of the solvent fraction and the solution viscosity due to the solvent's evaporation during spin-coating; B – Schematic phase diagram in a ternary

system of polystyrene blend with two molecular weights and solvent. The blue line separates the coexistence region from the spinodal decomposition region, illustrated by parallel lines. The arrows illustrate the system's path as the solvent evaporates with time, t_c is the time necessary to reach a critical concentration at which a two-phase region exists; 75/25, 50/50, 25/75 – different evaporation paths for the aforementioned polystyrene fractions.

3.1 Evaluation of solution viscosities

The viscosity measurement (Fig. 3.) can be used to assess not only the final coating thickness and the solvent evaporation time prediction, but also it can provide information about the character of polymer chains interactions. The measurement result is presented as reduced viscosity η_r/C, where C represents the concentration in mg/ml. Here $\eta_r = \frac{\eta - \eta_s}{\eta_s}$, where η is the dynamic viscosity of the solution and η_s is the viscosity of the solvent. In Fig. 3A, the viscosity is plotted as a function of the concentration.

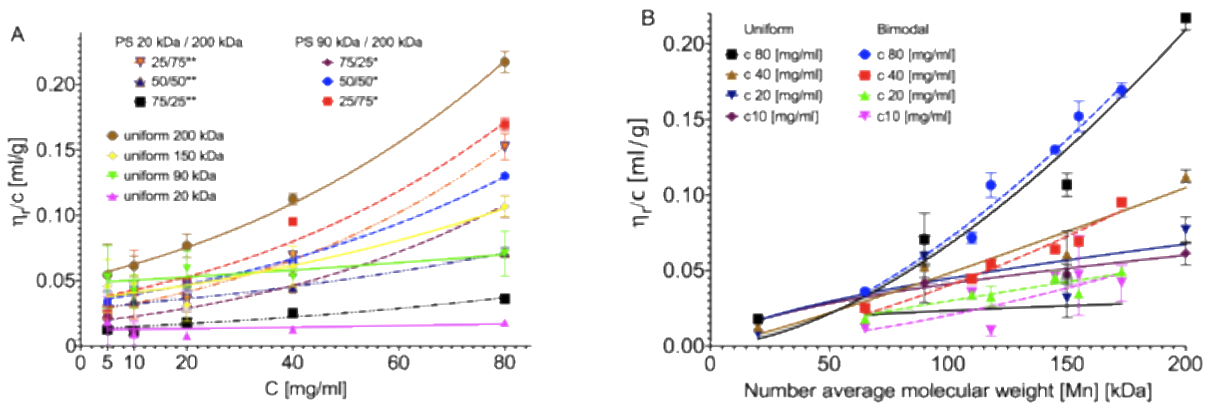

Fig. 3. Reduced viscosity η_r/C of the solutions, A - plotted against the solution's concentration, B in the number average molecular weight function, $[M_n] = f_1 M_{w1} + f_2 M_{w2}$, where f is w/w % ratio of polymers.

The general dependence of viscosity on concentration can be described in the form of a power series:(61)

$$\frac{\eta_r}{C} = [\eta](1 + K[\eta]C + \frac{K[\eta]C^2}{2} + \frac{K[\eta]C^3}{6}) \quad (2)$$

where $[\eta]$ is intrinsic viscosity at infinite dilution. The coefficients are summarised in Table S1 in SI. The intrinsic viscosity [η] was lower for bimodal blends. The difference between bimodal and uniform solution is visible for concentrations surpassing the overlap concentration at around 20 mg/ml.(62) It should be noted that the viscosity of the bimodal solutions increased faster with the increase of the concentration than in the case of uniform solutions. The K parameter was particularly high for 75/25 blends: 1.36 for 90 kDa and 200 kDa and 1.01 for 20 kDa and 200 kDa. In comparison, K for uniform 200 kDa was 0.36. Thus, it can be assumed that the number of the entanglements, attributed to the 200 kDa fraction, rises at higher concentrations. Fig. 3B presents the viscosity in relation to the number molecular weight [M_n]. The relation between viscosity and molecular weight can be described in the form of the Mark-Houwink equation:(61)

$$\frac{\eta_r}{C} = \ln K + a\ln[M_n]. \quad (3)$$

The *K* and [η] values are summarised in SI, Table S2. The uniform solutions were visibly more viscous than the bimodal counterpart of similar molecular weight. However, for 80 mg/ml, the difference disappeared, and the viscosity–molecular weight curves displayed similar tendencies. The bimodal solution ware less viscous than the uniform ones at low concentrations (C < 20 mg/ml), but viscosity increased at higher concentrations. It can be assumed that higher stress was applied to the longer polymer chains.

3.2 Evaporation of the solvent during spin-coating

Subsequently, the relation between the viscosity (concentrations C: 20 mg/ml, 40 mg/ml, and 80 mg/ml) of the uniform and bimodal solutions and the evaporation rate of the solutions during

spin-coating was analysed (Fig. 4). The in-situ reflectometry was used to measure the evaporation rate and investigate any particularities during the evaporation. The water droplet condensation coming from humidity depends on the temperature fluctuations related to the evaporation rate.

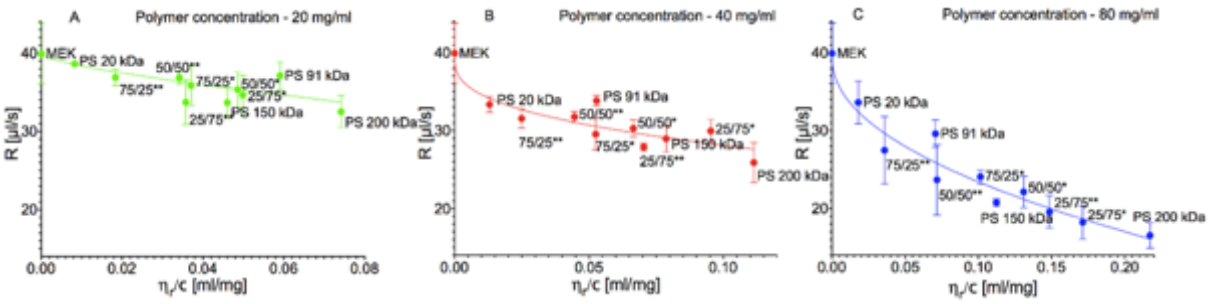

Fig. 4. The relation between the evaporation rate of solution and the reduced viscosity of solution for polymer concentrations: A - 20 mg/ml, B - 40 mg/ml, and C - 80 mg/ml, respectively.

Fig. 5A presents 1s of solvent evaporation in the form of a heat map. The heat map graph (Fig. 5A) presents the thinning rate of the solution (Δh/Δt) in µm/s, where the colour of each pixel corresponds to the thinning rate value. After 1s, the thickness of the film decreased enough for interference to cease. The shortest time was registered for pure MEK. The measured times increased accordingly to the average molecular weight of the solution. A clear region of a slower thinning was found in solutions with added higher molecular weight fraction after turbulent 0.3 s. The region spans between 0.3 s and 0.4 s. Fig. 5B presents an example of the evaporation curve of 50/50 w/w % 91 kDa and 200 kDa solution. Subsequently, the region of a lowered thinning rate is followed by a region of an increased thinning rate. This phenomenon can be assumed to be assigned to liquid-liquid phase separation on solvent and polymer-rich fraction. It is also possible that the addition of the longer chains facilitates this phase behaviour.

Then, the bimodal solutions' behaviour would be a mix of properties of its components acting as separate entities, as concluded from the viscosity examination.

On the other hand, this phenomenon can be associated with the final morphology formation. If so, the morphology would start to form in a relatively early stage of the process. Moreover, it can be assumed that the acceleration of evaporation in the later stage would be responsible for the decrease in surface temperature. This will subsequently facilitate water condensation.

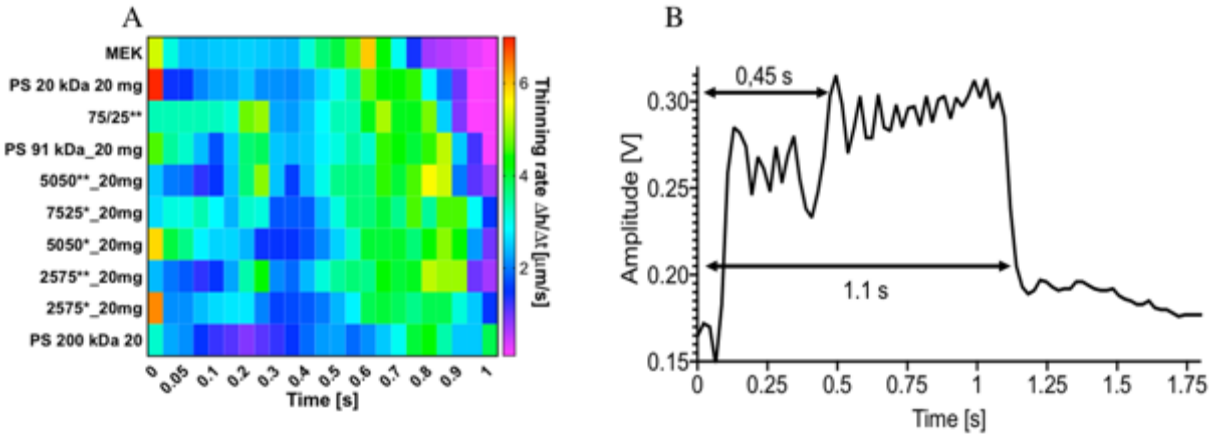

Fig. 5. A - Heat map of the thinning rate of the solution during the spin-coating for the concentration of 20 mg/ml; B – representative evaporation curve of 50/50 w/w % 91 kDa and 200 kDa solution, concentration 20 mg/ml, vertical axis corresponds to the voltage amplitude found on the photodetector. The horizontal axis corresponds to the duration of spin-coating.

3.3 Investigation of the thickness and morphology of the coatings spun at relative humidity 0%

The coatings spun at Rh 0% were chosen as a starting point for the investigation. We decided to look for phase separation if no humidity is applied, affecting the investigated solvent-polymer system. The convection Marangoni flow, solvent evaporation, and phase separation events alter the coating surface's morphology. As a result, the occurrence of wrinkles or arrays of islands on the coating surface was reported. (47,63–65)

The coatings were investigated via AFM and optical imaging to determine the effect of bimodal MWD on coating morphology. Significant differences between blend types occurred (Fig. 6A). The solution concentration of 80 mg/ml was chosen. As we expected from the mentioned above tests, the bimodal distribution role would be the highest. Moreover, we wanted to avoid the influence of the substrate on our force spectroscopy experiment. For that, we needed the thickest coating. As illustrated in Fig. 6B, the thickness of the coatings in the case of 80 mg/ml scaled linearly with the blends' average molecular weight.

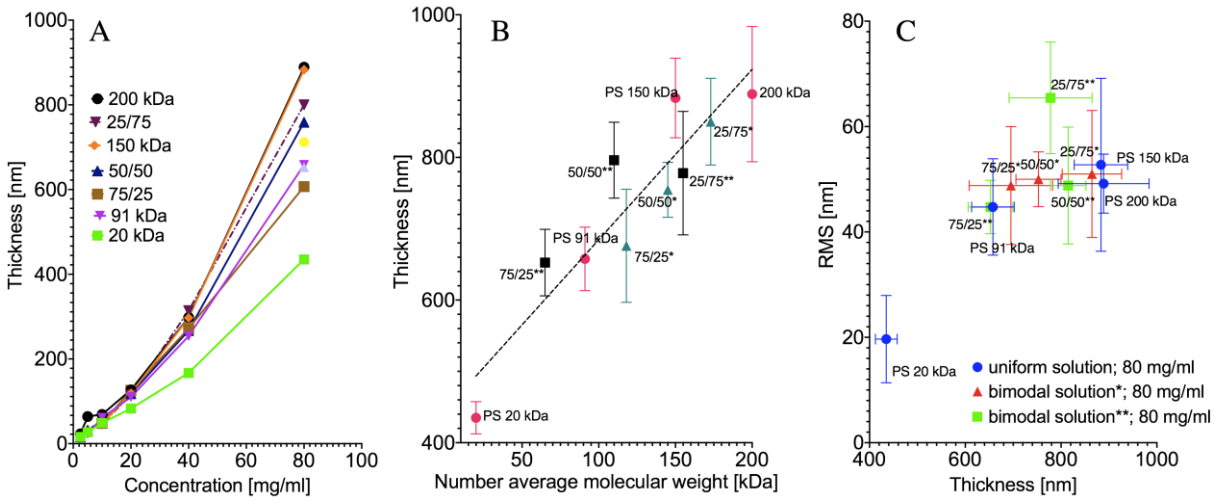

Fig. 6. A - Thickness of the coatings with respect to the composition and the concentration. The plot presents data for uniform and 91 kDa / 200 kDa solutions. B – Thickness of the coating for 80 mg/ml concentration in the blend's molecular weight function. * - Blends of 91 kDa and 200 kDa polystyrene; ** - blend of 20 kDa and 200 kDa polystyrene; x/x – w/w% ratio of blended homogeneous polystyrenes. The number average molecular weight [M_n] = $f_1M_{w1} + f_2M_{w2}$, where f w/w. % ratio of polymers. C - RMS roughness of the coatings spun from 80 mg/ml concentration.

Also, it was observed that roughness scales with the film's thickness, the values are not significantly different (Fig. 6C). Nonetheless, a similar RMS value can describe an infinite

number of possible morphologies. To represent the morphology of the material quantitatively, one can apply the Minkowski parameters.(66)

The images (Fig. 7A) used for analysis come from the central part of the image to exclude the high shear rate effect on the coating's morphology. Based on this description, it can be concluded that the morphology of the uniform coatings is characterised by separate islands (red colour in Fig. 7A) surrounded by a bicontinuous green phase. Oppositely, the bimodal coatings are characterised by a red bicontinuous phase with separate green islands included. The bicontinuous phase in such a case becomes fainter with the increase of the higher weight molecular fraction. This occurrence was observed in the case of both kinds of bimodal blends: 20 kDa / 200 kDa and 91 kDa / 200 kDa.

Fig. 7B presents boundary and connectivity. The first of the two parameters, boundary $B(\nu)$, characterises the number of bound pixels at the edge between dark and bright regions in a binarized picture at a specific threshold ν. Connectivity $C(\nu)$ can be used to describe the bicontinuous or island morphology of the coating in respect to the given binarization threshold ν. The negative value of connectivity corresponds to bicontinuous morphology, while the positive value corresponds to island morphology.

It thus states that the bimodal coatings had different morphology than the uniform coatings when the starting conditions (Rh 0%) are considered.

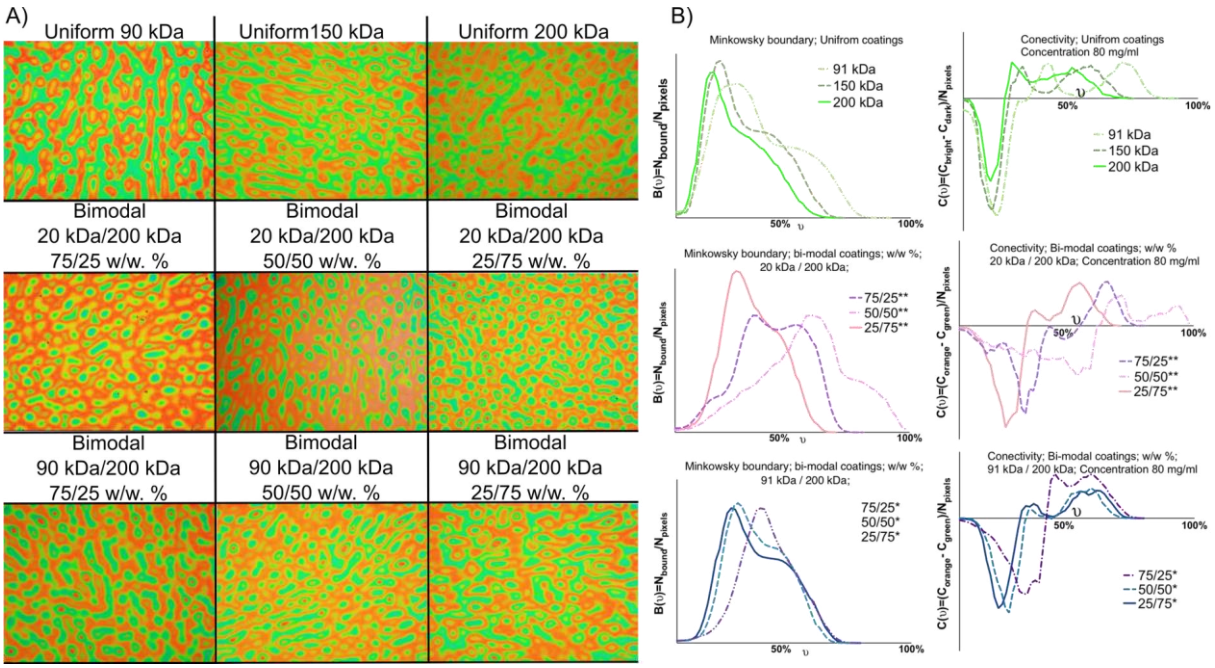

Fig. 7. A - Optical images of coatings spun from 80 mg/ml. The B- Minkowski boundary $B(\nu)$ and connectivity $C(\nu)$, of the coatings spun from 80 mg/ml, where ν represents the threshold for the image binarization, N_{bound} is the number of pixels bounded between bright and light picture areas at a given threshold, N_{pixels} is the total number of pixels, C_{orange} is a total number of orange pixels at a given threshold, C_{green} is the total number of green pixels at a given threshold.

3.4 Investigation of coatings phase composition by means of AFM Force Spectroscopy

AFM Force Spectroscopy method allows to visualise and quantify surface areas differing in mechanical properties.(67) The coatings spun from the solutions with a concentration of 80 mg/ml were studied. The resulting elastic modulus of the coatings was calculated (Fig. 8).

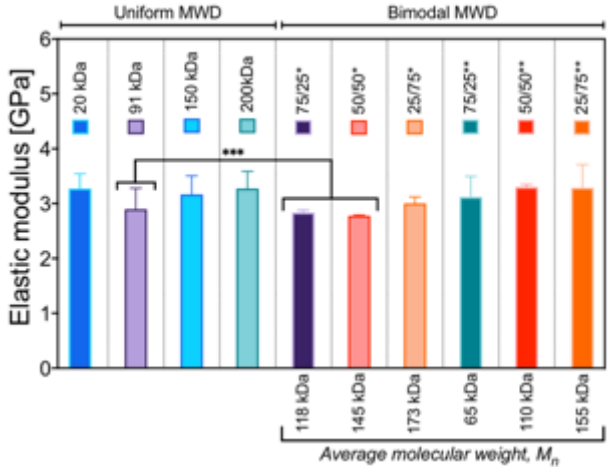

Fig. 8. Average elastic modulus obtained based on the FS method for coatings made from the solution of 80 mg/ml. Uniform – coatings were made from homogeneous solutions; Bimodal – coatings made from solutions with bimodal MWD; * - Blends of 91 kDa and 200 kDa polystyrene; ** - blend of 20 kDa and 200 kDa polystyrene; x/x – w/w% ratio of blended homogeneous polystyrenes. $[M_n] = f_1M_{w1} + f_2M_{w2}$, where f w/w % ratio of polymers. *** - means are significantly different (one-way ANOVA, $p < 0.05$).

The obtained results are similar to those found in the literature.(68) The uniform 91 kDa coating and the 75/25 and 50/50 blends of 91 kDa and 200 kDa had significantly lower elastic modulus than the rest of the tested groups. The dependence between the molecular weight and the elastic modulus of the polymer has been repeatedly proven.(69,70) However, we have not found significant differences between other groups than those mentioned. The uniform 20 kDa coating had a similar elastic modulus as the 200 kDa coating in our investigation. The 20 kDa coating was the thinnest thus, the substrate could influence the result. We have performed a linear regression test (SI, *Force Spectroscopy*, Fig. S4) between the thickness of the 80 mg/ml coatings and the elastic modulus, which proved no relationship between the thickness of the coatings and the elastic modulus, while the 20 kDa coating was an outlier (SI, *Force Spectroscopy*, Table 14).

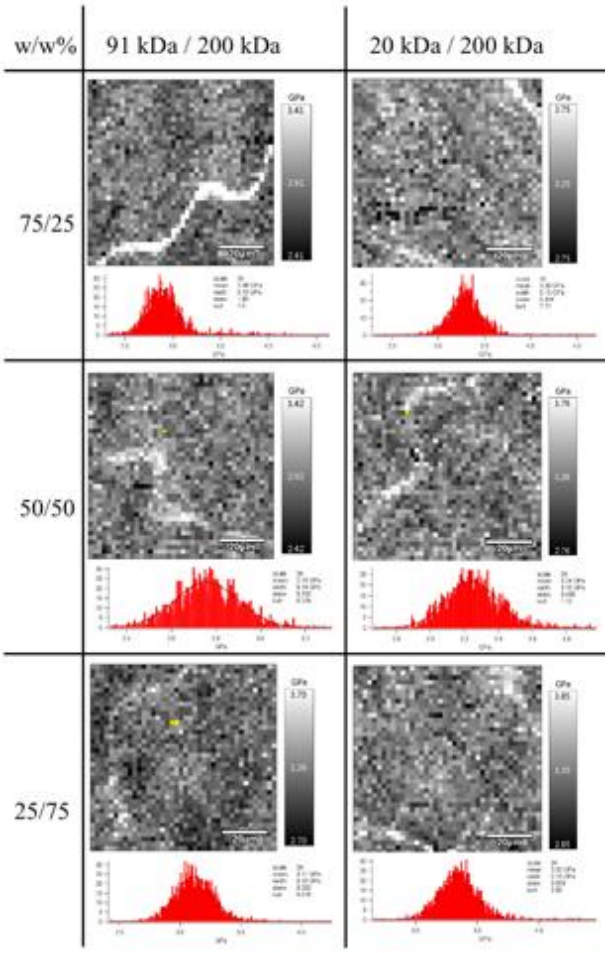

Fig. 9. Force Spectroscopy maps of bimodal MWD coatings. The greyscale shows the stiffness – the white colour corresponds to the highest stiffness. The grayscale range is ± 1 GPa.

Interestingly, it was possible to record local differences in the coating surface stiffness (Fig. 9). The maps were gathered for bimodal coatings. White spinodal-like areas are characterised by higher stiffness. The differences are more clearly visible in the case of 90 kDa and 200 kDa blends, in agreement with Fig. 8.

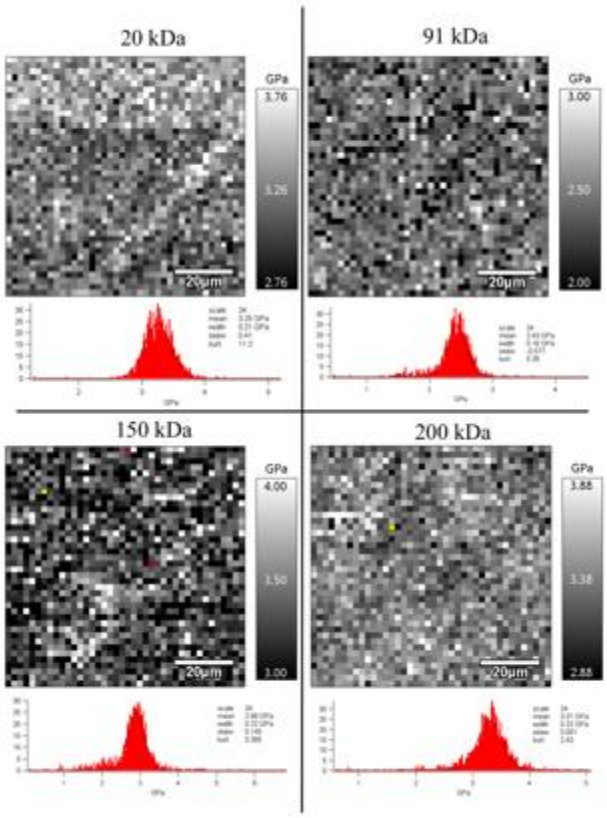

Fig. 10. Force Spectroscopy maps of coatings with uniform MWD. The greyscale shows the stiffness – the white colour corresponds to the highest stiffness. The grayscale range is ± 1 GPa.

For comparison, Fig. 10 illustrates the FS maps of the uniform coatings. We have analysed the skewness of the maps' elastic modulus distribution (SI, *Force Spectroscopy*, Table S15). The skewness in the case of uniform coatings was significantly lower ($p < 0.05$) than in the case of the bimodal coatings (Fig. 11). The distribution of the elastic modulus of the uniform coatings was more homogeneous.

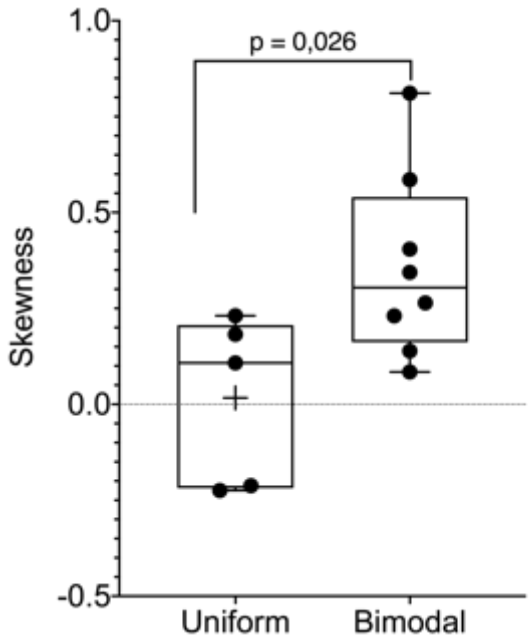

Fig 11. The skewness of the elastic modulus data sets. Uniform – grouped means that represents the skewness of histograms of uniform coatings elastic modulus. Bimodal – grouped means that represents the skewness of histograms of all kinds of bimodal blends elastic modulus. The means of these two groups are significantly different ($p < 0.05$).

Therefore, it was concluded that the force spectroscopy reviled the phase segregation in the bimodal coatings. The most noteworthy phase segregation was found for the 75/25 blends of both kinds of bimodal coatings. Here, the phase of lower concentration formed long, spinodal-like forms. While for the 25/75 blends, the separate phases were scattered.

3.5 Solubility of polystyrenes with respect to the molecular weight distribution

Those mentioned above phase segregation could be explained by solubility investigation. It was shown that the viscosity of the polymeric solution could be utilised by the application of the Mangaraj method to retract several polymer-solvent parameters, i.e. the Flory interaction parameter.(71) We utilised the Mangaraj equation (eq.4) to investigate the miscibility gap between the lower and the higher molecular weight polystyrenes.(72)

$$\ln\left(\frac{\eta}{\eta_{max}}\right) = -(\delta_s - \delta_{eff})^2. \quad (4)$$

The effective miscibility parameter δ_{eff} was calculated with respect to a solution of 200 kDa with a concentration of 80 mg/ml, which had the highest viscosity among the tested solutions (η_{max}). The solvent δ_s was set to be 19 $MPa^{0.5}$, which is a typical value for MEK.

The miscibility gap between low and high molecular weight polystyrene can be derived based on PS blends' viscosity. Furthermore, the miscibility gap decreases accordingly with the low molecular weight fraction. Here, δ_{eff} is the effective Hildebrand miscibility parameter calculated based on the intrinsic viscosity $[\eta]$. For the 20 mg/ml concentration, all the solutions are present on the same linear trend with the lowest δ_{eff} for the highest molecular weight. It should be noted that, with concentration increase, the trends for 20 kDa / 200 kDa solutions (brown squares), 91 kDa / 200 kDa solutions (purple triangles), and the uniform solutions (blue circles) become divergent at low molecular weights, with their trends being coincidental at 200 kDa.

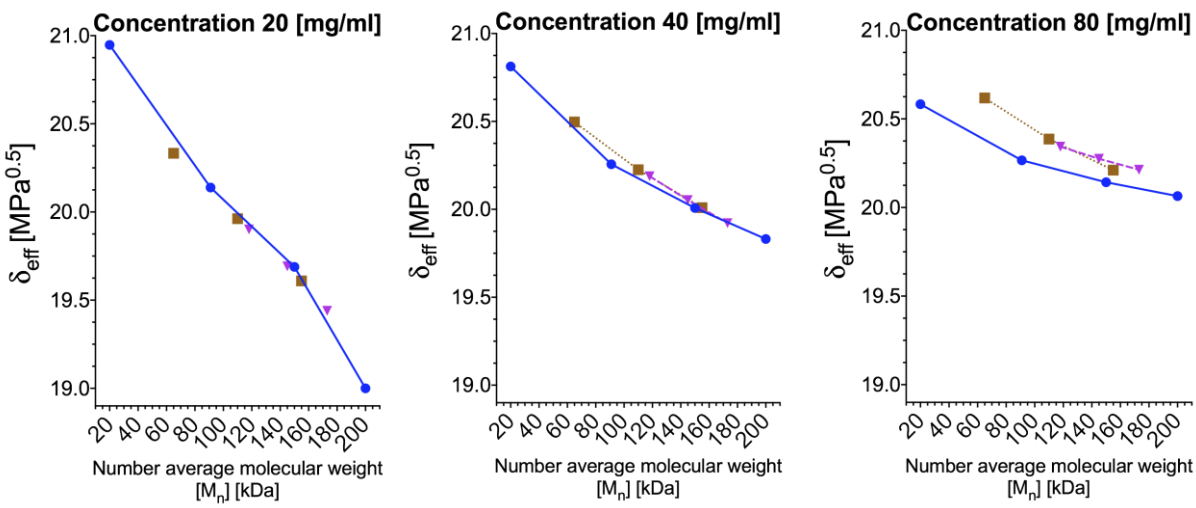

Fig. 12. The effective miscibility parameter δ_{eff} of the polystyrenes in MEK with bimodal and uniform distributions for two kinds of bimodal distributions: 20 kDa / 200 kDa – brown squares and 91 kDa / 200 kDa – purple triangles; the blue circles represent data for polystyrenes with the uniform distributions. $[M_n] = f_1 M_{w1} + f_2 M_{w2}$, where f w/w % ratio of polymers.

462

463 **3.5 Self-assembly of micropillars/honeycomb due to phase segregation and water**
464 **condensation**

465 As a follow-up, we have utilised the humidity to take advantage of the phase segregation
466 observed above. It was assumed that the phase segregation could be further enhanced if the
467 spin-coating would be performed in humid conditions. It was further concluded that the water
468 condensation would eventually lead to ruptures in the solution layer. By this, a new interface
469 between the solution, water, and SiO_2 substrate would be created. This would induce the
470 separation between segregated phases. The condensing water forces the liquid film to dewet
471 and retreat from SiO_2. The viscosity gradient between different phases would lead to the
472 formation of convection cells and honeycomb morphology.(73,74) It was assumed that the
473 spinodal-like structures found during the FS investigation, probably consisting of a higher
474 molecular weight fraction, would reinforce the honeycombs' borders. As was reviled by the
475 viscosity investigation, the longer polymer chains would carry the stress as they would be
476 highly entangled. The lower molecular phase would separate because no stress would be
477 applied to the shorter chains. It should also be considered that the MEK is a hygroscopic solvent
478 and while PS is slightly hydrophobic. The absorption of the water by MEK can further alter the
479 interactions between the solvent and different PS phases. The viscosity and solubility
480 investigations pointed to 80 mg/ml concentration to obtain the most pronounced effect. It was
481 also assumed that the water condensation would take place in the later stage of spinning. As the
482 humidity slows down the evaporation, the highest humidity would allow the longest time for
483 morphology formation. The tested relative humidity Rh values were 45%, 55%, 75%.

484 Fig. 13 A shows images of coatings composed of uniform polystyrenes, Fig. 13 B presents
485 images of coatings prepared from 91 kDa and 200 kDa blends, and Fig. 13 C presents images
486 of coatings prepared from 20 kDa and 200 kDa blends.

Each column is marked below with the mixture's PDI value, and each row corresponds to one of the Rh values. Optical microscope images show a larger area of the coatings and are presented in the Supplementary Information, Fig. S6 – S8.

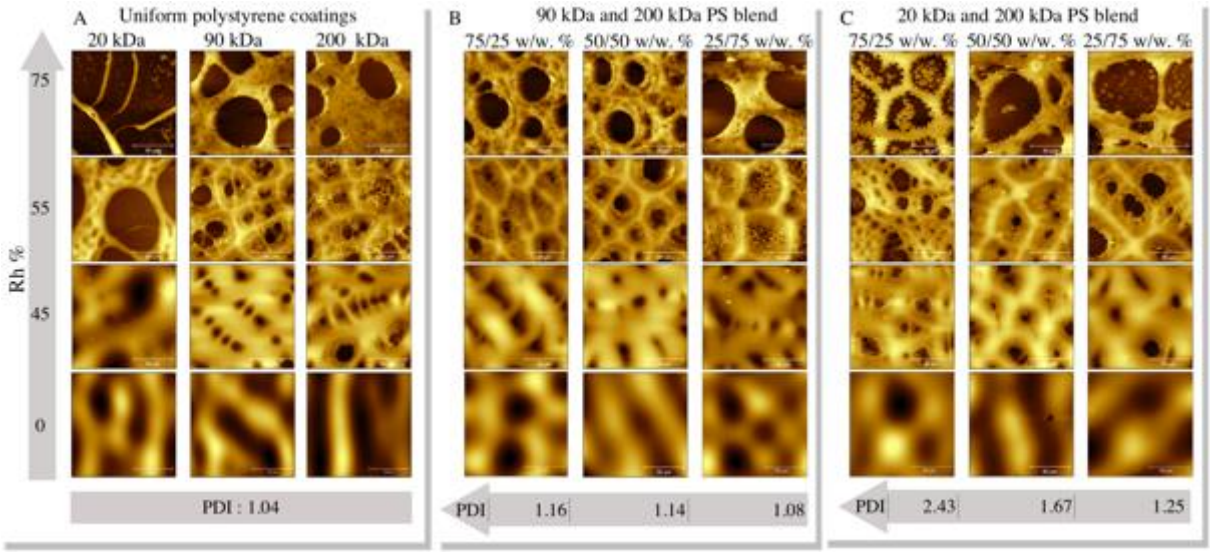

Fig. 13. Morphology of coatings with bimodal MWD spun under different humidity conditions, the solution concentration C was 80 mg/ml. The z-scale was chosen for the best representation of the coating's morphology. A – uniform coatings; B – 20 kDa and 200 kDa blends; C – 91 kDa and 200 kDa blends.

We have observed that the smaller cavities (breath figures) formed around, the larger cavities caused by dewetting related polymeric film ruptures. The structure which resembles the honeycomb also occurred. For Rh 55%, the honeycomb-like morphology is found for all coatings, except the uniform 20 kDa coating. Notably, the uniform coatings had lost their honeycomb morphologies when humidity Rh 75% was used. The bimodal coating of 91 kDa and 200 kDa, 25/75 w/w%, did not retain the honeycomb morphology. Probably, as shown by the FS, the spinodal structures were not formed for these coatings and could not reinforce the honeycomb borders. Radially averaged Power Spectra Density analysis (SI, Fig. S9) of

averaged four images depict the differences between the 75/25, 50/50, and 25/75 w/w% 20 kDa and 200 kDa coatings.

Interestingly, the coatings prepared from 20 kDa and 200 kDa bimodal blends at Rh 75% had polymeric pillars inside the large holes. The onset of such structures can also be observed in the case of coatings prepared in Rh 55%, but the length of the process, in this case, was too short for full pillar formation. The fraction of the pillars decreased with an increase of 200 kDa contribution. It was assumed that the pillars are made of a lighter and less viscous fraction. Seemingly, the heavier polymer fraction, more viscous and more entangled, reinforced the honeycomb cells borders.

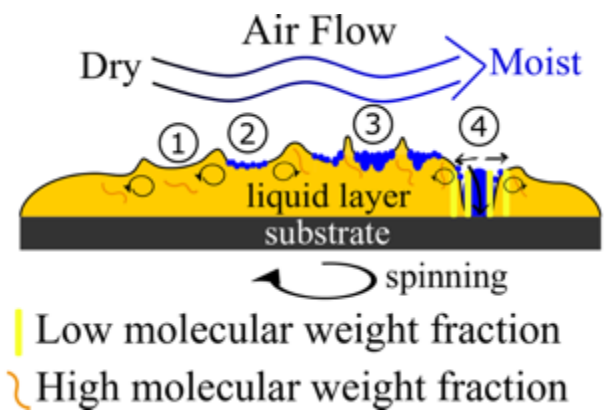

Fig. 14. Four scenarios of the phase segregation: spin-coating in dry air ((1), 0% Rh); moderate humidity ((2), 45% Rh; (3), 55% Rh); high humidity ((4), 75% Rh). Low and high molecular weight fractions, convective flow driving honeycomb formation, and low molecular weight separation at the boundary between the water-wetted region and the remaining liquid layer of the polymer solution are presented.

The scenarios mentioned above of coating at Rh 0%, 45%, 55%, and 75% are illustrated in Fig. 14. It was assumed that the blends underwent segregation before the condensation starts. The condensate water acted as a driving force that separated the two phases. The separation occurred at the solution/water/substrate interface.

Additionally, we had tested the formation of the micropillars when a short spin-coating time was used (0.5s and 1s). These images are presented in Fig. S15 in SI. The phase segregation was already seen, though the pillars were not well formed. These results would confirm the reflectometry experiment, which indicated that the phase separation could happen early on during the spin-coating.

The phase segregation was captured by the AFM image (Fig. 15 a-c). The black rectangle indicates the area that differed in terms of deflection signal and phase contrast. It was observed that cracks appeared between this area and the rest of the film. The water condensation forced the liquid PS film to dewet from the SiO_2. Black arrows mark the direction of dewetting. The low molecular weight segregated and separated from the main part of the film and formed pillars. As soon as the moisture fills the cracks, the separated material forms spherical structures due to the surface tension. The proposed mechanism of pillar formation is depicted in Fig 15 d.

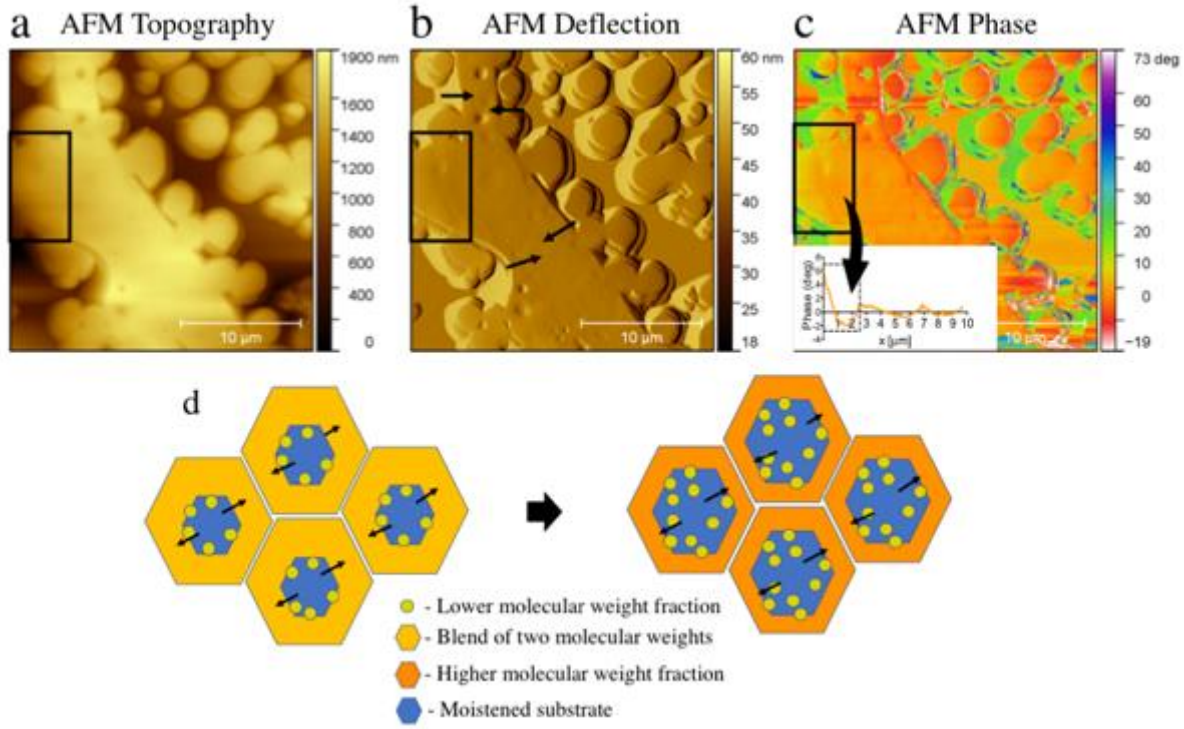

Fig. 15. AFM magnification of the cell border of the 20 kDa and 200 kDa 75/25 w/w% blend spun at Rh 75%. The black rectangle indicates the separation of different phases. The same

542 region is shown in the form of a - topography, b - AFM deflection, the direction of dewetting
543 is indicated by the black arrows; c - AFM phase image, an arrow indicates the phase signal
544 difference presented as the averaged cross-section of the marked region (black box); d –
545 schematic illustration depicting proposed pillar formation mechanism; Convection inside the
546 liquid film led to cells formation, condensation of water led to film rupture (Blue).
547 Subsequently, the recess of the film occurred. At the interface between the rupture area and the
548 receding film, segregation of lower molecular fraction arisen (Yellow). Subsequently, the cells'
549 borders were reinforced by the remaining high molecular weight fraction (Orange);
550
551 As was mentioned, the polystyrenes used were unmodified standard grade polymers. The
552 unchanged chemical composition of the coatings was confirmed by FTIR spectroscopy (SI Fig.
553 S10 – S12). The recognised functional groups were CH_3, CH_2, and phenyl groups. These groups
554 are hydrophobic and were the driving force behind the dewetting process under high humidity
555 conditions. This argument was further reinforced by the Free Surface Energy (SEF)
556 measurement (SI Fig. S13 – S14). The SEF of 20 kDa coating was slightly higher than the 200
557 kDa coating and, in consequence, lead to a higher affinity to the hydrophilic SiO_2 substrate of
558 the former one.
559
560 **Conclusions**
561 • The solutions' viscosity with bimodal blend distribution was lower than the uniform
562 solutions (< 20 mg/ml) but increased rapidly with the concentration. It was concluded
563 that the increase of the concertation increases the number of entangled longer polymer
564 chains (200 kDa fraction), and this fraction conveys the stress in the polymer film. The
565 lower molecular weight fraction (20 kDa or 90 kDa) acted as a separate entity.

- The viscosity data were applied to determine the solubility. It was concluded that if the mixture's polydispersity is high enough, i.e. 75/25 ration of lower to higher molecular weight fraction, both polystyrene blend components can act as separate species and segregate.
- The evaporation pattern during spin-coating and evaporation rate was characterised for each of the polystyrene blends. It was found that bimodal solutions have lowered evaporation rate at around 0.4 s of spin-coating and followed by an increase in evaporation.
- It was concluded that the internal thermal convection inside the bimodal films was different than for the uniform.
- The Force Spectroscopy revealed phase segregation. Spinodal-like features were found in the case of the bimodal coatings. These features were visible in both kinds of bimodal blends when the ratio was 75/25 %. However, for 25/75 % ratios, the phase segregation was more diffused, and the spinodal forms were not found.
- As the polystyrene is slightly hydrophobic, while the solvent (methyl ethyl ketone) is slightly hygroscopic, it was concluded that this could be utilised to increase the phase segregation. The humidity was used as a driving force to separate two phases of polystyrene. Coating in relative humidity of 45%, 55%, and 75% was tested. It was found that for 20 kDa and 200 kDa blend, the polystyrene segregated into pillars formed from the lower molecular weight fraction at the highest humidity. The higher molecular weight fraction formed the honeycomb cells. The higher molecular weight polystyrene acted as a frame for the formation of the pillars. The separation occurred at the solution/water/substrate interface.

The described mechanism can likely be applied to other solvent-polymer systems, consisting even of three polymer fractions. It is likely possible to apply the described process to other coatings methods, for example, dip coating, blade coating or ink-jet printing.

Supporting Information (SI)

Experimental setup depicting the custom build spin-coater with a humidity-controlled chamber and an in-situ reflectometer utilising stroboscopic effect. Illustration of thickness measurement. Viscosity-related coefficients. Optical microscope images. FTIR results. Free Surface Energy results.

Author information

Corresponding authors:

Maciej Łojkowski, ORCID: 0000-0002-0612-7964, email: 00183042@pw.edu.pl

Wojciech Swieszkowski, ORCID: 0000-0003-4216-9974, email: wojciech.swieszkowski@pw.edu.pl.

The authors declare no competing financial interest.

Acknowledgements

This manuscript is a part of Maciej Łojkowski PhD thesis. This work was supported by the National Centre for Research and Developments [STRATEGMED3/306888/3/NCBR/2017]. We are grateful Mgr. Donata Kuczyńska-Zemła for help with optical microscopy.

Authors contributions:

Conceptualization, M.Ł.; methodology, M.Ł., A.Ch., E.Ch.; investigation, M.Ł., A.Ch., E. Ch., imaging, M.Ł., A.Ch.; data analysis, M.Ł.; visualisation, M.Ł.; writing, M.Ł.; supervision, W. Ś.; revision of the manuscript, M.Ł., A.Ch., E. Ch., W. Ś; funding acquisition W. Ś. All authors have read and agreed to the published version of the manuscript.

Abbreviations

AFM – atomic force microscopy; bimodal – polymer with two nodes in molecular weight distribution; coating – final polymer coating; CA – Contact Angle; E – elastic modulus; film – liquid film of solution spread on the substrate; FS – force spectroscopy; FTIR – Fourier Transform IR; GPC – Gel permeation chromatography; initial solution – solution ate the start of spin-coating; MEK – Methyl Ethyl Ketone; Mw – molecular weight; [M_w] – Weight average molecular weight; [M_n] – Number average molecular weight; MWD – molecular weight distribution; PDI – Polydispersity index; PTF – Polymer thin film; PS – Polystyrene; Rh% - relative humidity in %; RMS – root mean square roughness; Uniform – polymer with one node in molecular weight distribution.

References

1. Kumar M, Bhardwaj R. Wetting characteristics of Colocasia esculenta (Taro) leaf and a bioinspired surface thereof. Sci Rep. 2020;10(1):1–15.
2. He R, Xiao J, Zhang M, Zhang Z, Zhang W, Cao Y, et al. Artificial honeycomb-inspired TiO2 nanorod arrays with tunable nano/micro interfaces for improving poly(dimethylsiloxane) surface hydrophobicity. J Mater Sci. 2016;51(6):2935–41.
3. Jahed Z, Shahsavan H, Verma MS, Rogowski JL, Seo BB, Zhao B, et al. Bacterial Networks on Hydrophobic Micropillars. ACS Nano. 2017;11(1):675–83.

4. Liu X, Liu R, Cao B, Ye K, Li S, Gu Y, et al. Subcellular cell geometry on micropillars regulates stem cell differentiation. Biomaterials [Internet]. 2016;111:27–39. Available from: http://dx.doi.org/10.1016/j.biomaterials.2016.09.023

5. Walheim S, Böltau M, Mlynek J, Krausch G, Steiner U. Structure Formation via Polymer Demixing in Spin-Cast Films. Macromolecules [Internet]. 1997 Aug 1;30(17):4995–5003. Available from: https://doi.org/10.1021/ma9619288

6. Daly R, Sader JE, Boland JJ. The dominant role of the solvent–water interface in water droplet templating of polymers. Soft Matter [Internet]. 2013;9(33):7960. Available from: http://xlink.rsc.org/?DOI=c3sm51452h

7. Khikhlovskyi V, Wang R, van Breemen AJJM, Gelinck GH, Janssen RAJ, Kemerink M. Nanoscale Organic Ferroelectric Resistive Switches. J Phys Chem C [Internet]. 2014 Feb 13;118(6):3305–12. Available from: https://pubs.acs.org/doi/10.1021/jp409757m

8. D'Andrade BW, Forrest SR. White Organic Light-Emitting Devices for Solid-State Lighting. Adv Mater [Internet]. 2004 Sep 16;16(18):1585–95. Available from: http://doi.wiley.com/10.1002/adma.200400684

9. Yabu H. Fabrication of honeycomb films by the breath figure technique and their applications. Sci Technol Adv Mater [Internet]. 2018;19(1):802–22. Available from: https://doi.org/10.1080/14686996.2018.1528478

10. Wu D, Xu F, Sun B, Fu R, He H, Matyjaszewski K. Design and Preparation of Porous Polymers. Chem Rev [Internet]. 2012 Jul 11;112(7):3959–4015. Available from: https://pubs.acs.org/doi/10.1021/cr200440z

11. Karagkiozaki V, Vavoulidis E, Karagiannidis PG, Gioti M, Fatouros DG, Vizirianakis IS, et al. Development of a nanoporous and multilayer drug-delivery platform for medical implants. Int J Nanomedicine. 2012;7(October):5327–38.

12. Calejo MT, Ilmarinen T, Skottman H, Kellomäki M. Breath figures in tissue engineering and drug delivery: State-of-the-art and future perspectives. Vol. 66, Acta Biomaterialia. 2018.

13. Vendra VK, Wu L, Krishnan S. Polymer Thin Films for Biomedical Applications. In: Nanotechnologies for the Life Sciences [Internet]. Weinheim, Germany: Wiley-VCH Verlag GmbH & Co. KGaA; 2011. Available from: http://doi.wiley.com/10.1002/9783527610419.ntls0179

14. Griesser HJ. Thin Film Coatings for Biomaterials and Biomedical Applications, 1st Edition. 2016. 310 p.

15. Łojkowski M, Walheim S, Jokubauskas P, Schimmel T, Święszkowski W. Tuning the wettability of a thin polymer film by gradually changing the geometry of nanoscale pore edges. Langmuir [Internet]. 2019;35(17):5987–96. Available from: https://doi.org/10.1021/acs.langmuir.9b00467

16. Plawsky JL, Kim JK, Schubert EF. Engineered nanoporous and nanostructured films. Mater Today [Internet]. 2009;12(6):36–45. Available from: http://dx.doi.org/10.1016/S1369-7021(09)70179-8

17. Bormashenko E. Breath-figure self-assembly, a versatile method of manufacturing membranes and porous structures: Physical, chemical and technological aspects. Membranes (Basel). 2017;7(3).

18. van Franeker JJ, Westhoff D, Turbiez M, Wienk MM, Schmidt V, Janssen RAJ. Controlling the Dominant Length Scale of Liquid-Liquid Phase Separation in Spin-coated Organic Semiconductor Films. Adv Funct Mater [Internet]. 2015 Feb;25(6):855–63. Available from: http://doi.wiley.com/10.1002/adfm.201403392

19. Schaefer C, Michels JJ, van der Schoot P. Structuring of Thin-Film Polymer Mixtures upon Solvent Evaporation. Macromolecules [Internet]. 2016 Sep 27;49(18):6858–70.

689 Available from: https://pubs.acs.org/doi/10.1021/acs.macromol.6b00537
690 20. Ebbens S, Hodgkinson R, Parnell AJ, Dunbar A, Martin SJ, Topham PD, et al. In Situ
691 Imaging and Height Reconstruction of Phase Separation Processes in Polymer Blends
692 during Spin Coating. ACS Nano [Internet]. 2011 Jun 28;5(6):5124–31. Available from:
693 https://pubs.acs.org/doi/10.1021/nn201210e
694 21. Danglad-Flores J, Eickelmann S, Riegler H. Deposition of polymer films by spin
695 casting: A quantitative analysis. Chem Eng Sci [Internet]. 2018 Apr;179:257–64.
696 Available from: https://linkinghub.elsevier.com/retrieve/pii/S0009250918300125
697 22. Daly R, Sader JE, Boland JJ. Taming Self-Organization Dynamics to Dramatically
698 Control Porous Architectures. ACS Nano [Internet]. 2016 Mar 22;10(3):3087–92.
699 Available from: https://pubs.acs.org/doi/10.1021/acsnano.5b06082
700 23. Müller-Buschbaum P, Gutmann JS, Wolkenhauer M, Kraus J, Stamm M, Smilgies D,
701 et al. Solvent-Induced Surface Morphology of Thin Polymer Films. Macromolecules
702 [Internet]. 2001 Feb;34(5):1369–75. Available from:
703 https://pubs.acs.org/doi/10.1021/ma0009193
704 24. Bornside DE. Spin Coating of a PMMA/Chlorobenzene Solution. J Electrochem Soc
705 [Internet]. 1991;138(1):317. Available from:
706 https://iopscience.iop.org/article/10.1149/1.2085563
707 25. Wodo O, Ganapathysubramanian B. Modeling morphology evolution during solvent-
708 based fabrication of organic solar cells. Comput Mater Sci [Internet]. 2012;55:113–26.
709 Available from: http://dx.doi.org/10.1016/j.commatsci.2011.12.012
710 26. Huang C, Förste A, Walheim S, Schimmel T. Polymer blend lithography for metal
711 films: Large-area patterning with over 1 billion holes/inch2. Beilstein J Nanotechnol.
712 2015;6(1):1205–11.
713 27. Wu BH, Zhong QZ, Xu ZK, Wan LS. Effects of molecular weight distribution on the

714 self-assembly of end-functionalized polystyrenes. Polym Chem. 2017;8(29):4290–8.
715 28. Jiang H, Zhang L, Qin J, Zhang W, Cheng Z, Zhu X. Producing bimodal molecular
716 weight distribution polymers through facile one-pot/one-step RAFT polymerization. J
717 Polym Sci Part A Polym Chem. 2012;50(19):4103–9.
718 29. Whitfield R, Parkatzidis K, Truong NP, Junkers T, Anastasaki A. Tailoring Polymer
719 Dispersity by RAFT Polymerization: A Versatile Approach. Chem [Internet]. 2020
720 Jun;6(6):1340–52. Available from:
721 https://linkinghub.elsevier.com/retrieve/pii/S2451929420301923
722 30. Tanaka K, Takahara A, Kajiyama T. Effect of Polydispersity on Surface Molecular
723 Motion of Polystyrene Films. Macromolecules [Internet]. 1997 Oct;30(21):6626–32.
724 Available from: https://pubs.acs.org/doi/10.1021/ma970057e
725 31. Zabusky HH, Heitmiller RF. Properties of high density polyethylenes with bimodal
726 molecular weight distribution. Polym Eng Sci. 1964;4(1):17–21.
727 32. Heitmiller RF, Naar RZ, Zabusky HH. Effect of homogeneity on viscosity in capillary
728 extrusion of polyethylene. J Appl Polym Sci [Internet]. 1964 Mar;8(2):873–80.
729 Available from: http://doi.wiley.com/10.1002/app.1964.070080226
730 33. Koningsveld R, Chermin HAG, Gordon M. Liquid─liquid phase separation in
731 multicomponent polymer solutions - VIII. Stability limits and consolute states in quasi-
732 ternary mixtures. Proc R Soc London A Math Phys Sci [Internet]. 1970 Oct
733 27;319(1538):331–49. Available from:
734 https://royalsocietypublishing.org/doi/10.1098/rspa.1970.0182
735 34. Zeman L, Patterson D. Effect of the Solvent on Polymer Incompatibility in Solution.
736 Macromolecules [Internet]. 1972 Jul;5(4):513–6. Available from:
737 https://pubs.acs.org/doi/abs/10.1021/ma60028a030
738 35. Shultz AR, Flory PJ. Phase Equilibria in Polymer—Solvent Systems1,2. J Am Chem

Soc [Internet]. 1952 Oct 1;74(19):4760–7. Available from: https://doi.org/10.1021/ja01139a010

36. Harris EK. Effect of blending on the rheological properties of polystyrene. J Appl Polym Sci [Internet]. 1973 Jun;17(6):1679–92. Available from: http://doi.wiley.com/10.1002/app.1973.070170604

37. Klein J. The Onset of Entangled Behavior in Semidilute and Concentrated Polymer Solutions. Macromolecules [Internet]. 1978 Sep;11(5):852–8. Available from: https://pubs.acs.org/doi/abs/10.1021/ma60065a002

38. Hong KM, Noolandi J. Theory of inhomogeneous multicomponent polymer systems. Macromolecules [Internet]. 1981 May;14(3):727–36. Available from: https://pubs.acs.org/doi/abs/10.1021/ma50004a051

39. Hariharan A, Kumar SK, Russell TP. A lattice model for the surface segregation of polymer chains due to molecular weight effects. Macromolecules [Internet]. 1990 Jul;23(15):3584–92. Available from: https://pubs.acs.org/doi/abs/10.1021/ma00217a009

40. Mahmoudi P, Matsen MW. Entropic segregation of short polymers to the surface of a polydisperse melt. Eur Phys J E [Internet]. 2017 Oct 6;40(10):85. Available from: http://link.springer.com/10.1140/epje/i2017-11575-7

41. Hill JA, Endres KJ, Mahmoudi P, Matsen MW, Wesdemiotis C, Foster MD. Detection of Surface Enrichment Driven by Molecular Weight Disparity in Virtually Monodisperse Polymers. ACS Macro Lett [Internet]. 2018 Apr 17;7(4):487–92. Available from: https://pubs.acs.org/doi/10.1021/acsmacrolett.7b00993

42. Stein GE, Laws TS, Verduzco R. Tailoring the Attraction of Polymers toward Surfaces. Macromolecules [Internet]. 2019 Jul 9;52(13):4787–802. Available from: https://pubs.acs.org/doi/10.1021/acs.macromol.9b00492

764 43. Carlier V, Sclavons M, Jonas AM, Jérôme R, Legras R. Probing Thermoplastic
765 Matrix−Carbon Fiber Interphases. 1. Preferential Segregation of Low Molar Mass
766 Chains to the Interface. Macromolecules [Internet]. 2001 May;34(11):3725–9.
767 Available from: https://pubs.acs.org/doi/10.1021/ma000404b
768 44. Suwa J, Kakiage M, Yamanobe T, Komoto T, Uehara H. Molecular Weight
769 Segregation on Surfaces of Polyethylene Blended Films as Estimated from
770 Nanoscratch Tests Using Scanning Probe Microscopy. Langmuir [Internet]. 2007
771 May;23(11):5882–5. Available from: https://pubs.acs.org/doi/10.1021/la070150o
772 45. Karim A, Slawecki TM, Kumar SK, Douglas JF, Satija SK, Han CC, et al. Phase-
773 Separation-Induced Surface Patterns in Thin Polymer Blend Films. Macromolecules
774 [Internet]. 1998 Feb;31(3):857–62. Available from:
775 https://pubs.acs.org/doi/10.1021/ma970687g
776 46. Hoppe H, Heuberger M, Klein J. Self-Similarity and Pattern Selection in the
777 Roughening of Binary Liquid Films. Phys Rev Lett [Internet]. 2001 May
778 21;86(21):4863–6. Available from:
779 https://link.aps.org/doi/10.1103/PhysRevLett.86.4863
780 47. Heier J, Kramer EJ, Revesz P, Battistig G, Bates FS. Spinodal Decomposition in a
781 Subsurface Layer of a Polymer Blend Film. Macromolecules [Internet]. 1999
782 Jun;32(11):3758–65. Available from: https://pubs.acs.org/doi/10.1021/ma981709h
783 48. Jandt KD, Heier J, Bates FS, Kramer EJ. Transient surface roughening of thin films of
784 phase separating polymer mixtures. Langmuir. 1996;12(15):3716–20.
785 49. Flory PJ, Höcker H. Thermodynamics of polystyrene solutions. Part 1.—Polystyrene
786 and methyl ethyl ketone. Trans Faraday Soc [Internet]. 1971;67:2258–69. Available
787 from: http://xlink.rsc.org/?DOI=TF9716702258
788 50. Imre A, Van Hook WA. Liquid-liquid demixing from solutions of polystyrene. 1. A

review. 2. Improved correlation with solvent properties. Vol. 25, Journal of Physical and Chemical Reference Data. 1996. p. 637–61.

51. Zgłobicka I, Chlanda A, Woźniak M, Łojkowski M, Szoszkiewicz R, Mazurkiewicz-Pawlicka M, et al. Microstructure and nanomechanical properties of single stalks from diatom Didymosphenia geminata and their change due to adsorption of selected metal ions. J Phycol. 2017;53(4).

52. Chlanda A, Kijeńska-Gawrońska E, Zdunek J, Swieszkowski W. Internal nanocrystalline structure and stiffness alterations of electrospun polycaprolactone-based mats after six months of in vitro degradation. An atomic force microscopy assay. J Mech Behav Biomed Mater [Internet]. 2020 Jan;101(August 2019):103437. Available from: https://linkinghub.elsevier.com/retrieve/pii/S1751616119305156

53. Sader JE, Borgani R, Gibson CT, Haviland DB, Michael J, Kilpatrick JI, et al. A virtual instrument to standardise the calibration of atomic force microscope cantilevers. Rev Sci Instrum [Internet]. 2016 Sep 1;87(9):093711. Available from: http://dx.doi.org/10.1063/1.4962866

54. Wu KC, You HI. Determination of solid material elastic modulus and surface energy based on JKR contact model. Appl Surf Sci. 2007;253(20):8530–7.

55. Toolan DTW. Straightforward technique for in situ imaging of spin-coated thin films . Opt Eng. 2015;54(2):024109.

56. Toolan DTW, Howse JR. Development of in situ studies of spin coated polymer films. J Mater Chem C. 2013;1(4):603–16.

57. Mokarian-Tabari P, Geoghegan M, Howse JR, Heriot SY, Thompson RL, Jones RAL. Quantitative evaluation of evaporation rate during spin-coating of polymer blend films: Control of film structure through defined-atmosphere solvent-casting. Eur Phys J E. 2010;33(4):283–9.

58. Heriot SY, Jones RAL. An interfacial instability in a transient wetting layer leads to lateral phase separation in thin spin-cast polymer-blend films. Nat Mater. 2005;4(10):782–6.

59. Drelich JW, Boinovich L, Chibowski E, Volpe C Della, Hołysz L, Marmur A, et al. Contact Angles: History of Over 200 Years of Open Questions. Surf Innov [Internet]. 2019;(March):1–25. Available from: https://www.icevirtuallibrary.com/doi/10.1680/jsuin.19.00007

60. Koningsveld R, Staverman AJ. Liquid–liquid phase separation in multicomponent polymer solutions. I. Statement of the problem and description of methods of calculation. J Polym Sci Part A-2 Polym Phys [Internet]. 1968 Feb;6(2):305–23. Available from: http://doi.wiley.com/10.1002/pol.1968.160060201

61. Utracki LA, Wilkie CA. Polymer blends handbook. Polymer Blends Handbook. 2014. 1–2378 p.

62. Ying Q, Chu B. Overlap concentration of macromolecules in solution. Macromolecules [Internet]. 1987 Mar;20(2):362–6. Available from: https://pubs.acs.org/doi/abs/10.1021/ma00168a023

63. Kim JK, Taki K, Nagamine S, Ohshima M. Periodic porous stripe patterning in a polymer blend film induced by phase separation during spin-casting. Langmuir. 2008;24(16):8898–903.

64. Heier J, Kramer EJ, Groenewold J, Fredrickson GH. Kinetics of individual block copolymer island formation and disappearance near an absorbing boundary. Macromolecules. 2000;33(16):6060–7.

65. Coveney S, Clarke N. Pattern formation in polymer blend thin films: Surface roughening couples to phase separation. Phys Rev Lett. 2014;113(21):1–5.

66. Mecke K. Additivity, Convexity, and Beyond: Applications of Minkowski Functionals

in Statistical Physics. Stat Phys Spat Stat [Internet]. 2000;111–84. Available from: http://link.springer.com/chapter/10.1007/3-540-45043-2_6

67. Wolf BA. Improvement of polymer solubility: Influence of shear and of pressure. Pure Appl Chem. 1997;69(5):929–33.

68. Du B, Tsui OKC, Zhang Q, He T. Study of Elastic Modulus and Yield Strength of Polymer Thin Films Using Atomic Force Microscopy. Langmuir [Internet]. 2001 May;17(11):3286–91. Available from: https://pubs.acs.org/doi/10.1021/la001434a

69. Landel RF, Nielsen LE. Mechanical properties of polymers and composites. CRC press; 1993.

70. Torres JM, Stafford CM, Vogt BD. Impact of molecular mass on the elastic modulus of thin polystyrene films. Polymer (Guildf) [Internet]. 2010;51(18):4211–7. Available from: http://dx.doi.org/10.1016/j.polymer.2010.07.003

71. Kok CM, Rudin A. Prediction of Flory–Huggins interaction parameters from intrinsic viscosities. J Appl Polym Sci. 1982;27(2):353–62.

72. Lee SH, Lee SB. The Hildebrand solubility parameters, cohesive energy densities and internal energies of 1-alkyl-3-methylimidazolium-based room temperature ionic liquids. Chem Commun. 2005;(27):3469–71.

73. Bormashenko E, Malkin A, Musin A, Bormashenko Y, Whyman G, Litvak N, et al. Mesoscopic patterning in evaporated polymer solutions: Poly(ethylene glycol) and room-temperature-vulcanized polyorganosilanes/-siloxanes promote formation of honeycomb structures. Macromol Chem Phys. 2008;209(6):567–76.

74. Uchiyama H, Matsui T, Kozuka H. Spontaneous Pattern Formation Induced by Bénard–Marangoni Convection for Sol–Gel-Derived Titania Dip-Coating Films: Effect of Co-solvents with a High Surface Tension and Low Volatility. Langmuir [Internet]. 2015 Nov 17;31(45):12497–504. Available from:

https://pubs.acs.org/doi/10.1021/acs.langmuir.5b02929